

Anisotropic Kitaev Spin Glass in $\text{Li}_2\text{Ru}_x\text{Ir}_{1-x}\text{O}_3$

Mayia A. Vranas,^{1,*} Alejandro Ruiz,² Vikram Nagarajan,³ Erik Lamb,¹ Gerald D. Morris,⁴ Zahir Islam,⁵ Christie Nelson,⁶ Benjamin A. Frandsen,⁷ James G. Analytis,⁸ and Alex Frano¹

¹Department of Physics, University of California, San Diego, California 92093, USA

²Department of Physics, University of California, San Diego, California, 92093, USA

³Institute of Science and Technology Austria, 3400 Klosterneuburg, Austria

⁴Centre for Molecular and Materials Science, TRIUMF, Vancouver, British Columbia, Canada V6T 2A3

⁵Advanced Photon Source, Argonne National Laboratory, Argonne, Illinois 60439, USA

⁶National Synchrotron Light Source II, Brookhaven National Laboratory, Upton, New York 11973, USA

⁷Department of Physics and Astronomy, Brigham Young University, Provo, Utah 84602, USA

⁸Department of Physics, University of California, Berkeley, California 94720, USA

(Dated: February 3, 2026)

Kitaev iridates have been proposed as candidates for realizing an elusive quantum spin liquid (QSL) state, in which strong spin-orbit coupling and bond-directional exchange generate a highly frustrated and entangled ground state. However, all physical systems proposed to host this ground state, including Li_2IrO_3 , Na_2IrO_3 , and RuCl_3 , develop magnetic order at low temperatures due to competing interactions. Nonetheless, theoretical modeling of experimental data has shown that Kitaev interactions are still present, motivating the application of perturbations such as pressure, magnetic field, and chemical doping to drive the system into the QSL phase. Here we study $\beta\text{-Li}_2\text{Ru}_x\text{Ir}_{1-x}\text{O}_3$ with dilute levels of Ru, $x \lesssim 10\%$. Through a combination of magnetometry, resonant elastic X-ray scattering, *ac*-heat capacity, and muon spin relaxation/resonance, we show that weak magnetic disorder suppresses long-range antiferromagnetic order and stabilizes an anisotropic spin glass that retains key signatures of Kitaev exchange. This Kitaev spin glass shows pronounced directional anisotropy in its magnetic susceptibility and thermoremanent magnetization. These results demonstrate that dilute magnetic disorder can access an anisotropic Kitaev spin glass: a proximate phase that freezes the Kitaev frustration landscape. This could provide a new window into the degeneracy, anisotropy, and competing interactions underlying the Kitaev QSL.

I. INTRODUCTION

In quantum materials, the spin degree of freedom provides an ample platform for the exploration of novel ground states and emergent phenomena. A great deal of attention has been put on the quantum spin liquid (QSL), in which the electron spins are both highly frustrated and entangled, leading to a dynamic superposition ground state [1]. The Kitaev honeycomb model for a QSL in particular has been lauded for its potential [2–5], as it is exactly solvable, possesses exotic Majorana excitations, and is realizable in a number of physical systems, among them RuCl_3 [6] and the Kitaev honeycomb iridates, A_2IrO_3 (A=Li,Na) [7, 8].

In the honeycomb iridates, the building blocks for the Kitaev model are the Ir^{4+} ions confined in oxygen octahedra (Fig. 1a), where crystal electric field splitting and strong spin-orbit coupling lead to a $J_{eff} = 1/2$ moment. The arrangement of these octahedra in an edge-sharing honeycomb configuration leads to three competing planes of interaction, the so-called Kitaev directions. By splitting the $J_{eff} = 1/2$ moments into itinerant and localized Majorana particles, a single, exactly soluble QSL ground state is achieved, in which all spin configurations are entangled and weighed equally [2, 3, 9].

This particular arrangement is achieved in the honeycomb Kitaev iridates $\alpha, \beta, \gamma\text{-Li}_2\text{IrO}_3$ and Na_2IrO_3 , as well as in their cousin compound RuCl_3 , where Cl^- replaces the O^{2-} in the octahedral cage. However, long-range magnetic order is seen in all of these compounds at low temperatures [10–14], indicating other interactions are at play. An extended model was developed to span the numerous magnetic ground states in these materials which includes both a direct exchange J between the Ir moments, and an off-diagonal indirect exchange Γ [3]:

$$H = \sum_{\langle ij \rangle \in \alpha\beta(\gamma)} [J\vec{S}_i \cdot \vec{S}_j + KS_i^\gamma S_j^\gamma + \Gamma(S_i^\alpha S_j^\beta + S_i^\beta S_j^\alpha)] \quad (1)$$

A phase diagram in which (J, K, Γ) are parameterized as $(\sin \theta \cos \phi, \sin \theta \sin \phi, \cos \theta)$, depicted in Fig. 1c, shows how changing the weights of these different interactions can lead to the diverse magnetic states seen in the physical compounds [4, 15]. The goal in achieving a Kitaev QSL in these materials then becomes finding ways to tune these interaction strengths, suppressing J and Γ sufficiently so that K dominates. An especially interesting candidate for this is $\beta\text{-Li}_2\text{IrO}_3$, a three-dimensional honeycomb iridate with twists in the honeycomb plaquettes (Fig. 1a) [16], which achieves an incommensurate spiral magnetic ground state at low temperatures, proximate to the QSL [11]. This phase additionally shows a high-temperature anomaly at T_η with the application of weak magnetic fields, which has a ferromagnetic character and is attributed to the onset of Kitaev exchange

* mvranas@ucsd.edu

interactions [17].

Many studies have been conducted attempting to identify and tune the parameters of β -Li₂IrO₃, creating the pressure-field-temperature phase diagram pictured in Fig. 1b. In applying relatively weak magnetic fields of $H^* = 2.4$ T, a change in slope is seen in the magnetization, which resonant elastic X-ray scattering (REXS) studies have shown corresponds to the onset of a zigzag phase [18]. This implies a decrease in the ϕ term in the theoretical diagram from $\phi > 3\pi/2$ to $\phi < 3\pi/2$ (black arrow in Fig. 1c), effectively weakening J and strengthening K , while leaving Γ unchanged. High pressure studies, meanwhile, show that T_N remains unchanged up to 1.4GPa, at which point the Ir–Ir bond lengths are sufficiently short to produce dimerization that suppresses the low-temperature ground state [19, 20].

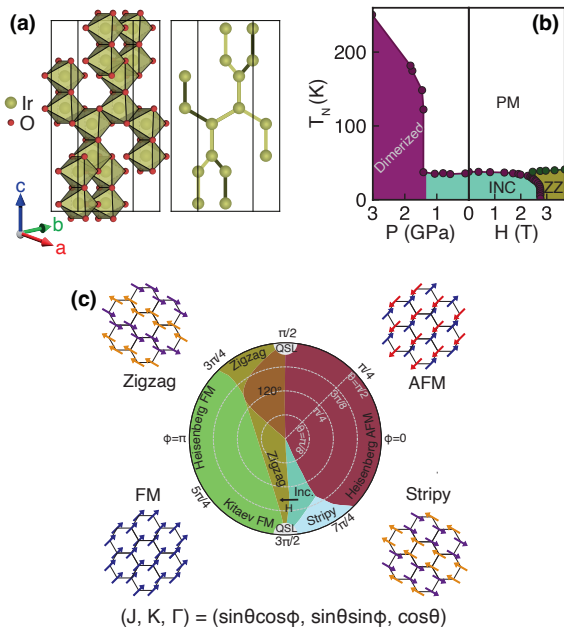


FIG. 1: (a) Crystal structure of β -Li₂IrO₃. Li ions are omitted for visibility. Ir-O octahedra form a twisted honeycomb structure (right). (b) Phase diagram for β -Li₂IrO₃ as a function of pressure and applied field, from [18–20]. (c) Phase diagram of the JKT model, with schematics of different spin configuration. The black arrow shows the effect of applied magnetic field, which moves the system from the incommensurate state to the zigzag state. Reproduced from [4, 15].

Chemical doping provides an additional means to tune the magnetic order, either by introducing charge carriers, altering bond lengths, or introducing magnetic disorder. Theoretical modeling has shown that magnetic- and charge-doped Kitaev iridates can achieve a variety of states and properties, including topological superconductivity for hole-dope iridates [21–23], a spin glass state for magnetic impurity or deficiency doping [24–26], flux binding in single impurities [27], and a Kondo effect for

spin- S impurities [28]. Experimental studies have followed up on these predictions. Low levels of Li substituted onto the Na sites of Na₂IrO₃ lead to a spiral magnetic state, which evolves into a spin glass at low doping [29], although further work saw phase separation that may alter these results [30]. On the high Li-side of the doping spectrum, a suppression of T_N is seen [31]. Meanwhile, doping Ti on the magnetic Ir sites in Na₂IrO₃ and Li₂IrO₃ [32], and Ru on the Ir sites in Na₂IrO₃ [26], leads to a spin glass state for dilute dopings. Ru doping in Li₂IrO₃ has previously been shown to suppress the AFM transition, and bond dimers emerge for higher Ru dopant levels [33].

However, progress in understanding the effects of disorder in β -Li₂IrO₃ has been limited by the difficulty of obtaining single-crystalline samples with dilute chemical substitution, particularly at impurity levels low enough to perturb a metastable magnetic ground state without destroying it. As a result, prior studies of doped Li₂IrO₃ have been restricted almost exclusively to polycrystalline samples, precluding direct access to directional anisotropies that are central to Kitaev physics. Previous work discussed above [33] has shown that higher levels of Ru substitution on the Ir sites, i.e. Li₂Ru_xIr_{1-x}O₃ with substitution increments $\Delta x = 10\%$, leads to a suppression of the magnetic ground state at low Ru concentrations. However, the intermediate regime between antiferromagnetic order and paramagnetism remains unexplored, as well as any potential anisotropic response inherent to the underlying exchange interactions [33].

In this work, we aim to overcome these limitations by synthesizing single crystals of β -Li₂Ru_xIr_{1-x}O₃ with dilute Ru substitution ($x \lesssim 10\%$), enabling a detailed investigation of the disorder-driven evolution of magnetism at low impurity concentrations. Pristine Li₂RuO₃ is expected to have an antiferromagnetic ground state due to the ordering of $S = 1$ moments on the Ru³⁺ sites, which is observed in single crystals [34]. However, theoretical modeling and experimental studies have also shown a tendency for the Ru³⁺ sites to dimerize, forming a valence bond liquid [35, 36]. In studying dilute doping in Li₂Ru_xIr_{1-x}O₃, we assume that dimerization is minimal, and instead treat the Ru³⁺ sites as magnetic $S = 1$ impurities. Using a combination of SQUID magnetometry, *ac*-heat capacity, REXS, and muon spin relaxation/resonance (μ SR), we demonstrate that dilute magnetic disorder does not simply suppress magnetic order, but rather stabilizes an anisotropic spin glass that preserves the bond-directional character of Kitaev exchange. This reveals a previously inaccessible regime in which glassy freezing emerges from a highly frustrated, anisotropic magnetic manifold, rather than from conventional random exchange.

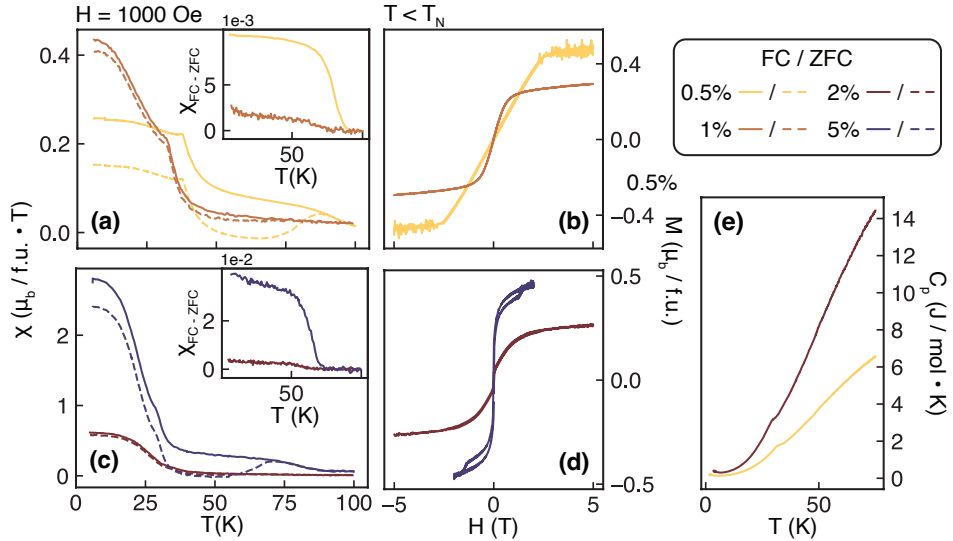


FIG. 2: (a) Field-cooled and zero-field cooled magnetic susceptibility for the ultra-low doping regime, $x \sim 0.5\%, 1\%$, with inset showing $\Delta\chi_{FC} - \chi_{ZFC}$. A suppression of T_N and T_η and an increase in the total moment is seen, as expected with the doping of a $S = 1$ ion. (b) Magnetization as a function of applied field for the ultra-low doping regime shows a decrease in H^* with increased doping. (c-d) In the low doping regime, T_N and T_η are further suppressed. A large increase in both the magnitude of the susceptibility and the FC-ZFC splitting is seen for $x \sim 5\%$. This may be explained by the spin-flop transition appearing for $x \sim 5\%$, indicating that moments are aligning to the applied field even for very small H . (e) The *ac*-heat capacity for the ultra-low and low doping regimes shows a pronounced feature at T_N , which becomes broader for higher dopings.

II. METHODS

High-quality single crystals of $\text{Li}_2\text{Ru}_x\text{Ir}_{1-x}\text{O}_3$ were grown by a two-step solid-state reaction. First, Li_2RuO_3 was synthesized by reaction of pure Ru (99.9% purity, BASF) and Li_2CO_3 (99.999% purity, Alfa-Aesar) powders in the molar ratio of 1:1.05 for 84hr at 1010°C, followed by cooling to room temperature at 7°C/hr. In the second step, Ir (99.9% purity, BASF) and Li_2CO_3 (99.999 % purity, Alfa-Aesar) powders were ground in a 1:1.05 stoichiometric ratio. Li_2RuO_3 powder was added with mass calculated using:

$$m_{LRO} = m_{\text{Li}_2\text{CO}_3/\text{Ir Powder}} \cdot \frac{M_{LRO}}{M_{LIO}} \cdot \frac{x}{1-x}$$

where m are mass in grams, M is molar mass, and x is the desired Ru percentage. The ground powder was pressed into a pellet, reacted in an alumina crucible for 84hr at 1010°C, and cooled to room temperature at 7°C/hr. Single crystals of $\text{Li}_2\text{Ru}_x\text{Ir}_{1-x}\text{O}_3$ were then extracted from the reacted powder. While energy-dispersive X-ray spectroscopy (EDS) was conducted on single crystals, results were inconclusive for nominal doping below 5% Ru. Therefore, all Ru levels stated are extrapolated from nominal doping levels from synthesis and trends in the T_N and T_η .

Field- and temperature-dependent magnetization were studied using a Quantum Design MPMS3 SQUID. Both field cooled (FC) and zero-field cooled (ZFC) magnetic

susceptibility was studied, by cooling the sample with and without a magnetic field, and measuring through a heating cycle with an applied field of 1000Oe.

The *ac*-specific heat $C_{ac}(T, H)$ measurements were conducted using a 16 T Cryogenic CFMS, which detects how the sample's temperature changes in response to an oscillating heater power. For this, a sample is placed over six thermocouples connected in series under a free-standing silicon nitride membrane $\sim 1\mu\text{m}$ thick. An *ac* current with frequency ω is driven through an adjacent resistive heater, resulting in an oscillating power, $P_{ac} = 1/2 I_o^2 R \cdot (1 + \cos(2\omega t))$. The temperature of the sample V_{ac} oscillates at a frequency 2ω and can be used to calculate the *ac*-heat capacity:

$$C_{ac} \sim \frac{P_{ac}}{\omega \cdot V_{ac}} \quad (2)$$

These measurements were performed in a low pressure He-4 gas environment ($\sim 10\text{mbar}$). The optimal frequency used in this experiment was 20 Hz, necessary to ensure that the thermal link through the membrane and the gas can be ignored, and that the sample is heated homogeneously.

Magnetic REXS measurements were conducted at the Ir L_3 edge ($E = 11.215\text{keV}$) on single crystals of $\text{Li}_2\text{Ru}_x\text{Ir}_{1-x}\text{O}_3$. These studies were conducted at both the Advanced Photon Source (APS) at beamline 6-ID-B and at the National Synchrotron Light Source II (NSLS II) at beamline 4-ID with vertical scattering geometry

using a σ -polarized incident beam.

μ SR experiments were conducted at TRIUMF Laboratory to investigate the emergent glassy behavior seen in $\text{Li}_2\text{Ru}_x\text{Ir}_{1-x}\text{O}_3$. In a μ SR experiment, spin-polarized, positively charged muons are implanted one at a time in the sample, where they typically come to rest at an interstitial position, undergo Larmor precession in any local magnetic field present at the stopping site, and subsequently decay into positrons after a mean lifetime of $\sim 2.2\ \mu\text{s}$. Pairs of detectors are placed on opposite sides of the sample to detect the positrons, which are emitted preferentially in the direction of the muon spin at the moment of decay. The experimental quantity of interest is the time-dependent asymmetric distribution of positrons detected by each detector in the pair, computed as

$$a(t) = (N_1(t) - N_2(t))/(N_1(t) + N_2(t)) \quad (3)$$

where $N_1(t)$ and $N_2(t)$ are the numbers of positrons incident on each detector at time t after muon implantation. The asymmetry is proportional to the spin polarization of the muon ensemble projected onto the axis defined by the detectors, providing direct access to the local magnetic field distribution in the sample [37]. Powder samples with nominal compositions $x = 0, 0.01, 0.05, 0.08$, and 0.1 were investigated using the LAMPF spectrometer on the M20D endstation. A helium gas flow cryostat with a base temperature of $\sim 1.8\ \text{K}$ was used to control the temperature.

III. RESULTS

In substituting less than 10% Ru on the Ir sites of $\beta\text{-Li}_2\text{IrO}_3$, a trend emerges in which both the low-temperature T_N and the high-temperature T_η , marked by a slope change in magnetic susceptibility and a splitting of the FC-ZFC magnetic susceptibilities, respectively, are suppressed to lower temperatures. Because precisely measuring dopant levels below 10% is challenging using existing methods (such as EDS and X-ray diffraction), we instead use these trends in the suppression of T_N , nominal Ru content used in synthesis, and comparison to previous studies on higher Ru content [33]. Based on these trends, we present representative behaviors in three regimes: ultra-low doping ($x \lesssim 1\%$), low doping ($1\% \lesssim x \lesssim 5\%$), and mid-doping ($5\% \lesssim x \lesssim 10\%$).

A. Ultra-low and low doping regimes ($x \lesssim 5\%$)

At ultra-low levels of Ru, a slight suppression of a few Kelvin is seen in both T_N and T_η , with an initial increase in the total susceptibility. This is also reflected in the $M - H$ loops, where the transition to the zigzag phase at H^* occurs at lower applied fields. This indicates that in this regime, the dopants are already destabilizing the incommensurate ground state (Fig. 2a-b).

As Ru content is increased to the low doping regime, the magnitude of χ increases further, while T_N, η continue to be pushed to lower temperatures (Fig. 2c). The high-temperature FC-ZFC splitting becomes more pronounced, and a spin-flop transition occurs at $x \sim 5\%$ (Fig. 2d), implying that, at sufficiently high doping, the antiferromagnetically ordered regime is destabilized enough to allow moments to align with the applied magnetic field. Still, there is a discontinuity in the *ac*-heat capacity in both regimes which reflects T_N , indicating that antiferromagnetic order is remains present (Fig. 2e).

To explore the impacts of doping in the ultra-low and low doping regimes on the magnetic propagation vector, REXS was conducted (Fig. 3). These studies indicate that the antiferromagnetic propagation vector, which has a value of $\vec{q} = (0.567, 0, l)$ for even l in pristine $\beta\text{-Li}_2\text{IrO}_3$, is still present with a small, non-systematic variation in the center position of h . The magnetic peaks for each dopant level, pictured in Fig. 3b-d, emerge at T_N , in agreement with values extracted from magnetic susceptibility. The small variation in h , along with the suppression in T_N (Fig. 3f), indicates that the Ru content may act to destabilize the magnetically ordered state, in particular impacting the off-diagonal Γ exchange interaction. A relative change in the off-diagonal exchange was indeed predicted to alter the incommensurate \vec{q} [15]. No magnetic Bragg peaks indicating stripy or zigzag phases were found in the region of reciprocal space that was explored.

B. Mid doping regime ($5\% \lesssim x \lesssim 10\%$)

As the Ru content is increased further, new behavior begins to emerge. For $x \gtrsim 5\%$, only one transition is observed, in which there is a pronounced FC-ZFC splitting at low temperatures, and a narrow, S-shaped hysteresis in the $M - H$ curves (Fig. 4a-b). The kink at H^* is no longer present, implying that the system does not move into the zigzag phase with applied field. The jump in *ac*-heat capacity is also less pronounced, though a broad feature is seen near T_F , where the FC-ZFC curves split (Fig. 4c). While REXS studies were conducted on a single crystal of $x \sim 10\%$, no magnetic peaks were apparent at the incommensurate, stripy, or zigzag sites.

Combined, these behaviors indicate that a glassy phase may be present. Due to the small sample size, standard *ac*-magnetic susceptibility measurements were not possible. Instead, time-dependent measurements were conducted to study the relaxation of the magnetic susceptibility. Ordered spontaneous symmetry breaking states tend to respond rapidly upon the application and removal of a magnetic field, returning to their ordered ground states within seconds or minutes. However, in a glassy phase, the “rugged” energy landscape requires more traversal of phase space to find a low-energy configuration, so spin glasses are quantified by a thermoremanent magnetization (TRM) that persists to long timescales

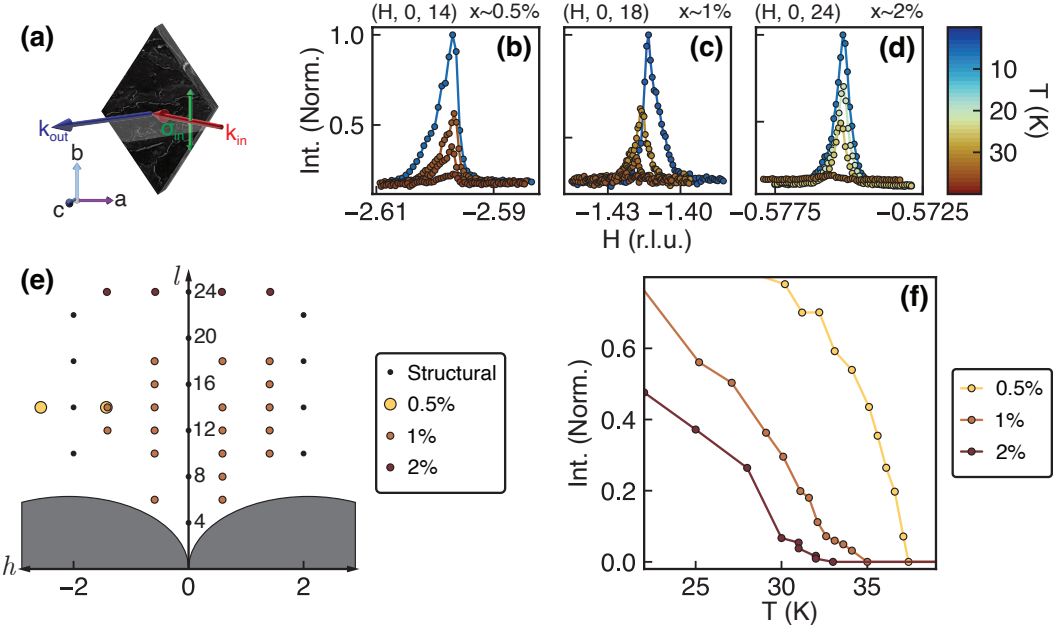


FIG. 3: (a) Diagram depicting the scattering geometry for REXS experiments. A vertical scattering geometry was used, such that the incident beam k_{in} is polarized along σ_{in} perpendicular to the scattering plane. (b-d) Peak profiles as a function of temperature for characteristic magnetic Bragg reflections seen in $x \sim 0.5\%$, 1% , 2% samples. Variations in alignment restricted which peaks were accessible, so different peaks were studied for each sample. Intensity is normalized to the peak intensity of the lowest measured temperature. (e) Mapping of the magnetic Bragg reflections $(h, 0, l)$ seen in REXS experiments for different samples. Black circles indicate lattice reflections, while orange, yellow, and red circles correspond to signals seen for different dopants. (f) Self-normalized temperature dependence of the magnetic peak intensity. T_N found in scattering are consistent with those derived from magnetometry.

[38]. To measure this TRM, the system was cooled without field below the glassy or antiferromagnetic transition, after which a field of 1T was applied for a fixed amount of time. This field was then removed, and the magnetization was measured for 75 min. Fig. 4d shows a scaled version of these curves, which have been normalized and offset to reflect how long it takes for the system to go from its initial to the lowest measured magnetization after 10 min in a 1T field. The decay was fit to an exponential, from which the characteristic timescale τ was extracted:

$$M = Ae^{-t/\tau}. \quad (4)$$

For samples in the ultra-low doping regime, a faster relaxation is seen, with $\tau \lesssim 10$ min, requiring less than ten minutes for the spins to relax into their ordered phase. As doping increases above $x \sim 5\%$, a sharp upturn is seen in the relaxation time, with τ reaching 38 min for $x \sim 10\%$ (Fig. 4f).

Another indicator of the glassy state is the dependence of the decay rate on the amount of time for which the field is applied. This is because, when a field is applied for longer to a spin glass, the spins have more time to settle into a particular ground state, and more spin flips are required to settle into a lower-energy configuration after

the field is removed. This effect is most pronounced for $x \sim 10\%$ at a temperature of 5K, where a field was held at 2, 5, or 10 mins. As the duration of field application is increased, a slower relaxation rate is seen, in line with the spin glass model (Fig. 4e,g).

Further evidence of glassy behavior for the moderately doped samples is found in the μ SR data. As large sample volumes were required, polycrystalline powder samples were utilized. In a μ SR experiment conducted in zero applied field (ZF), shown schematically in Fig. 5a, the time-dependent asymmetry $a(t)$ takes characteristic shapes depending on the nature of the magnetic state [39]. For long-range-ordered magnetic ground states, the ZF asymmetry shows coherent oscillations with time due to the presence of well-defined local fields at the muon stopping sites, where the width of the field distribution is proportional to the damping rate of the oscillations. This is observed for the ZF asymmetry spectra collected from the $x = 0\%$ and $x \sim 1\%$ samples at 2K, shown in Fig. 5b. Both spectra can be fit well using a sum of zeroth-order Bessel functions of the first kind, which is the expected lineshape for incommensurate magnetic order [40], exactly consistent with the known magnetic ground state in the low doping limit. The faster damping rate in the

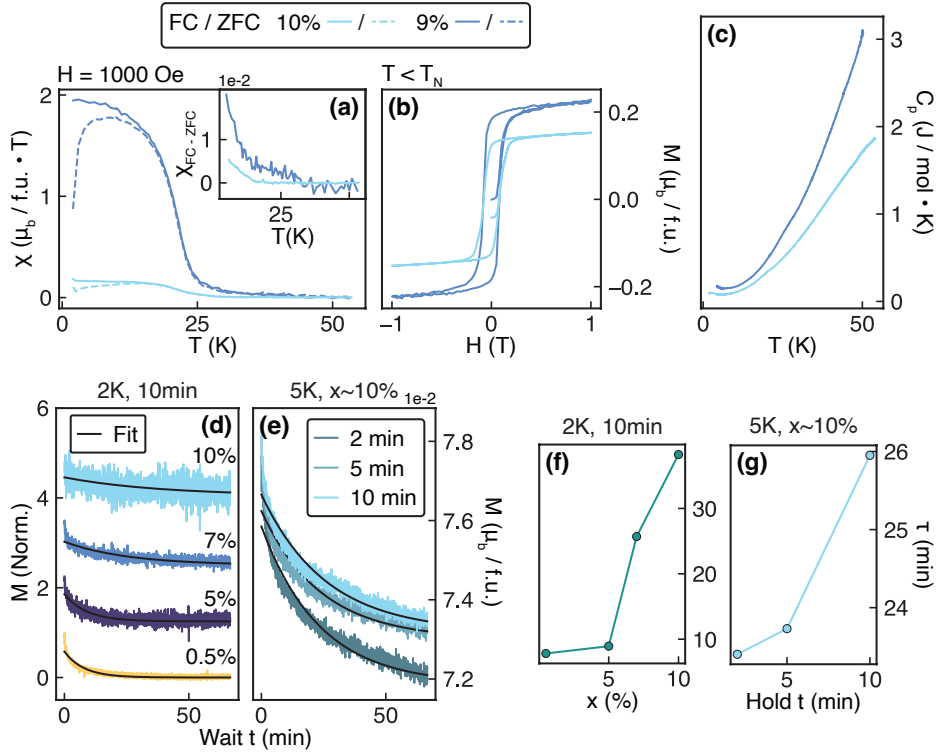


FIG. 4: (a) Magnetic susceptibility in the mid-doping regime, with inset showing the difference between FC and ZFC susceptibility. (b) M vs. H shows an opening of a hysteresis and the absence of the kink field H^* . (c) The ac-heat capacity shows a broad feature at T_f , indicative of a spin glass. (d) Thermoremanent magnetization (TRM) as a function of doping after holding in a 1T field at 2K for 10min. A longer relaxation time is seen for higher dopings. (e) TRM for $x \sim 10\%$ at 5K with varying hold times at 1T. A longer relaxation time is seen for longer hold times. (f,g) Characteristic timescale extracted from exponential fits of (d,e). Higher doping levels correspond to longer characteristic timescales. In the glassy (mid-doping) regime, longer hold times also lead to longer characteristic timescales.

$x \sim 1\%$ sample points to a broader field distribution at the muon stopping sites compared to the undoped sample, attributable to dopant-induced disorder. In contrast, the spectra for $x \gtrsim 5\%$ (Fig. 5b) show only an initial dip in asymmetry followed by a gradual recovery. This overdamped behavior, referred to as the Kubo-Toyabe (KT) lineshape, is a hallmark of spin glasses [39] and arises from the distribution of static, random fields at the muon stopping sites. The spectra can be well fit by the sum of two KT functions. When a longitudinal field (LF) is applied, the initial decrease in asymmetry is suppressed, as seen in Fig. 5e for the $x \sim 8\%$ sample. This “decoupling” of the asymmetry demonstrates that the ZF relaxation is due to static magnetic fields as opposed to dynamically fluctuating fields, again consistent with a spin glass ground state. Taken together, the ZF and LF μ SR spectra demonstrate clearly the doping-driven transition from incommensurate order to a spin glass ground state.

Investigating the temperature-dependent transition into the spin glass ground state is also illuminating. We show this for the $x \sim 8\%$ compound in Fig. 5(c), where

representative ZF spectra collected between 2 K and 50 K are displayed. At high temperature, the spectra exhibit slow, Gaussian-like relaxation, consistent with a paramagnetic state. As the temperature decreases, a fast front-end relaxation appears, indicating the presence of static magnetic fields at the stopping positions of some of the muons. The growth of this fast front end is proportional to the fraction of the sample volume with static magnetic fields, i.e. the volume fraction of the spin glass state. At sufficiently low temperatures, the Gaussian-like component is completely eliminated, leaving only the KT spin glass relaxation, indicative of a 100% spin glass volume fraction. The temperature dependence of the spin glass fraction extracted from our fits to the μ SR spectra is shown in Fig. 5(d), demonstrating a gradual, volume-wise transition from the paramagnetic state to the spin glass ground state. The temperature range of the transition is consistent with the magnetometry data.

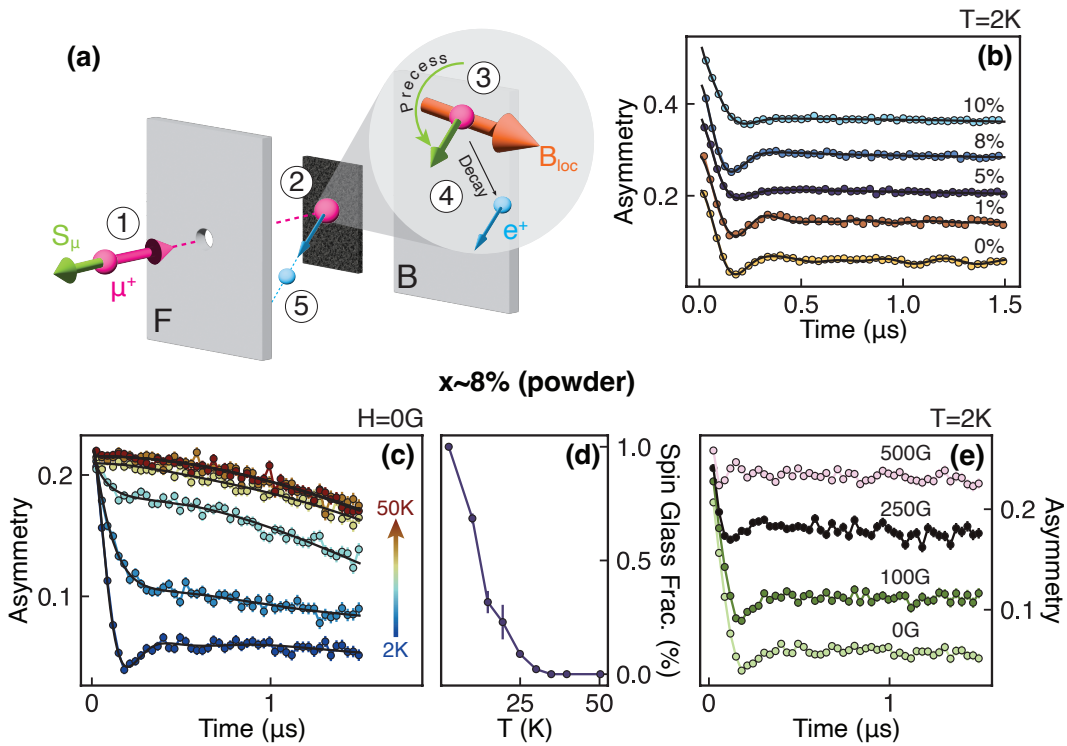


FIG. 5: (a) Schematic representation of a typical μ SR experiment. (1) Spin-polarized muons are sent into the sample chamber, with their spin angular momentum opposite to their direction of motion. (2) A muon implants itself into the material. (3) The spin of the implanted muon precesses in the local magnetic field. (4) The muon decays into a positron, which is emitted preferentially in the direction of the muon's spin. (5) The positron is detected by the front or back detectors. The normalized difference between the number of muons detected over time by these detectors is the measured asymmetry. (b) Asymmetry as a function of time after muon implantation for different dopings, collected at 2 K. Coherent oscillations are seen in the pristine and ultra-low dopings, consistent with long-range incommensurate order, while overdamped behavior characteristic of a spin glass state is seen for higher dopings. The spectra for subsequent dopings are offset vertically for clarity. (c) Asymmetry spectra for $x \sim 8\%$ in zero field collected at different temperatures. (d) From fits to the curves in (c), the volume fraction of the spin glass state is extracted, showing a T_g roughly consistent with the magnetometry data. (e) Asymmetry spectra for $x \sim 8\%$ at 2K as a function of applied longitudinal field, showing a steady recovery of asymmetry with increasing field as expected for a static spin glass ground state.

IV. DISCUSSION

The emergence of spin glass behavior upon doping a Kitaev interaction-dominant system is not unusual. In $\text{Na}_2\text{Ru}_x\text{Ir}_{1-x}\text{O}_3$, doping of $x = 5\%$ and above induces a spin glass [26]. In $\text{A}_2\text{Ti}_x\text{Ir}_{1-x}\text{O}_3$ ($\text{A}=\text{Na,Li}$), a spin glass also emerges in both compounds with the lowest levels of nonmagnetic Ti substitution [32]. These studies emphasize the importance of short-range coupling in Na_2IrO_3 , as the magnetic order is easily perturbed by magnetic and non-magnetic impurities; even in the case of doping Li on the cation sites of Na_2IrO_3 , the impact on the lattice parameters sufficiently disorders the local exchange interactions to drive the system into a spin glass state. However, in Li_2IrO_3 , even though a spin glass does emerge for low dopings, Θ_{CW} is unaffected, indicating that impurities do not disrupt the exchange interactions

to the same extent as in Li_2IrO_3 [32].

This means that in Li_2IrO_3 , though the magnetically ordered state is extremely fragile to perturbation, the long-range exchange pathways are robust. The spin glass that results from magnetic and non-magnetic impurity doping appears to relieve degeneracy without disrupting long-range magnetic correlations. In $\text{Li}_2\text{Ru}_x\text{Ir}_{1-x}\text{O}_3$, this leads to a unique anisotropic quality in the resulting spin glass, as is presented in Fig. 6a-b.

This anisotropy can be compared to the case of $\text{Ru}_{1-x}\text{Cr}_x\text{Cl}_3$, where $S = 3/2$ moments from Cr^{3+} replace the $J_{eff} = 1/2$ moments of the Ru^{3+} ions. For dilute Cr doping, a reversal of the magnetic anisotropy is seen, such that the easy axis moves from the direction perpendicular to the basal plane to the basal plane [41]. The anisotropy seen in $\text{Ru}_{1-x}\text{Cr}_x\text{Cl}_3$ can be explained by the ferromagnetic Heisenberg-type Cr-Cr exchange inter-

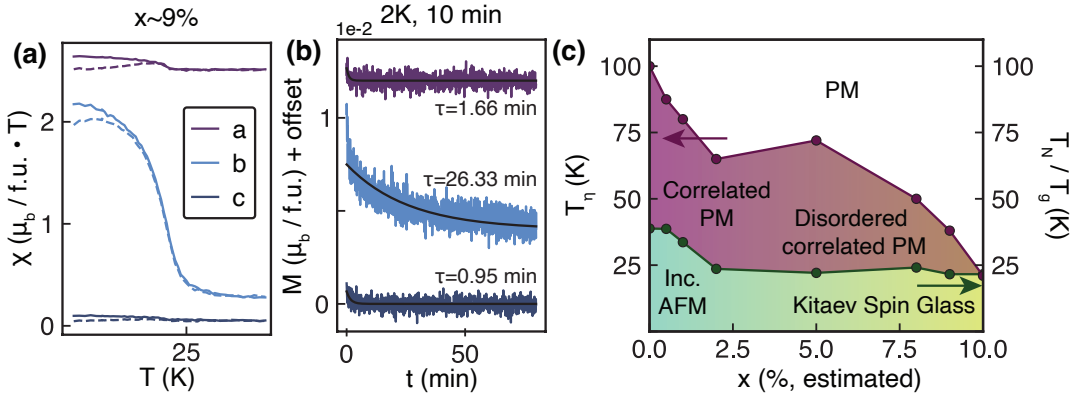


FIG. 6: (a) Magnetic susceptibility of $x \sim 9\%$ with $H = 1000$ Oe applied along a, b, c , with the b -axis remaining the easy axis even in the spin glass state. (b) TRM for the same sample with $H = 1$ T applied along a, b, c at $T = 2$ K for 10 min. Exponential fits show that when the field is applied along b , the system takes longer to stabilize into a magnetic ground state. (c) Proposed phase diagram for $\text{Li}_2\text{Ru}_x\text{Ir}_{1-x}\text{O}_3$ with $x \lesssim 10\%$. T_n is extracted from the upturn in χ_{FC-ZFC} , while T_N/T_G is extracted by inspecting $d\chi/dT$.

actions, which would prefer to align to an out-of-plane applied field. By comparison, the anisotropy present in the spin glass regime of $\text{Li}_2\text{Ru}_x\text{Ir}_{1-x}\text{O}_3$ is unique in part because it reflects the anisotropy of the pristine system, maintaining the b -axis as its easy axis. This is in agreement with the notion that in Li_2IrO_3 , long-range exchange pathways are robust to local perturbations. Furthermore, the properties of the glassy phase itself maintain the pristine Li_2IrO_3 anisotropy, as can be seen in the TRM (Fig. 6b). In applying and subsequently removing a field of $H = 1000$ Oe to the crystalline a, b, c -axes, a slower characteristic timescale τ for the relaxation is seen when the field is applied along the b -axis. This indicates that the spins participating in the spin glass are the same as those responsible for the anisotropic behavior. Anisotropy in a spin glass, while not unprecedented [42–44], is unusual, and to our knowledge this is the first time spin glass anisotropy has been seen in a compound with Kitaev-like interactions.

One interpretation of the above results can be viewed in terms of the $JK\Gamma$ compass model. In the pristine system, the presence of J and Γ disrupt the frustrated state such that an incommensurate magnetic ground state emerges. The suppression of T_N upon doping indicates that one or both of these terms is becoming weaker, such that the system does not magnetically order as readily. The weakening of J or Γ is further supported by the appearance of a spin-flop transition at $x \sim 5\%$, where a ferromagnetically aligned state as appears on the left side of Fig. 1c emerges with applied field, reducing the amount of time the system would spend in the zigzag phase. By this interpretation, as the doping increases, only the Kitaev-like interaction would remain significant, creating the elusive Kitaev QSL. However, the addition of disorder is also sufficient to lift the degeneracy of spin configurations, thereby inducing a Kitaev spin glass around

$x \sim 8\%$.

It is reasonable to assume that all exchange couplings, including K , would be weakened by dilute doping; however, previous doping experiments do indicate that the long-range Kitaev correlations are robust to perturbations, and therefore may not be as impacted as the short-range Heisenberg-like interactions J . The anisotropy of the Kitaev spin glass further point to remnant Kitaev interactions, with their frustration relieved by the random, dilute doping, creating a glass.

It should also be noted that this description does not account for the specific interactions between Ru-Ir and Ru-Ru sites. The behavior of $S = 1$ Ru^{4+} ions on a honeycomb lattice itself is non-trivial, with theoretical modeling [35] and experimental studies [36] indicating that the Ru^{4+} sites dimerize via orbital overlap due to orbital degeneracy to form a valence bond liquid, though single-crystalline studies have also shown an antiferromagnetically ordered state [34]. In either case, it is reasonable to assume that a Heisenberg-type interaction dominates for both Ru-Ru and Ru-Ir exchanges in a dilutely doped system. Despite this added complexity, the effective impact on the J, K, Γ couplings appears to sufficiently describe the behavior of the doped system. This hypothesis, based on the data presented here, could be further investigated by additional experiments. For example, REXS under applied magnetic field may be conducted on $x \sim 5\%$ samples to determine if a zigzag state is still achieved, as in [18]; and, resonant inelastic X-ray scattering (RIXS) can show if changes in the magnetic excitation spectrum are in agreement with reduced non-Kitaev coupling strengths [45].

V. CONCLUSION

In conclusion, we use a combination of magnetometry, *ac*-heat capacity, magnetic REXS, and μ SR to study the evolution of $\text{Li}_2\text{Ru}_x\text{Ir}_{1-x}\text{O}_3$ from an incommensurate antiferromagnet to an anisotropic Kitaev spin glass. We show through magnetic susceptibility and TRM that the anisotropy of the pristine system is preserved in the glassy state, indicating that Kitaev exchange interactions are maintained with low doping levels, and the disruption of the frustration from these interactions with disorder is responsible for the resulting spin glass. These results indicate that the implantation of magnetic impurities may be a key method to achieve a Kitaev QSL.

VI. ACKNOWLEDGMENTS

We thank Nicolas Ducharme, Alec Petersen, and Alex Shaw for assistance with the μ SR data collection. We

also thank Yi-Zhuang You for useful discussions. This material is based upon work supported by the National Science Foundation under Grant No. DMR-2145080. M.A.V. acknowledges support from the National Science Foundation Graduate Research Fellowship under Grant No. DGE-2038238. This research used beamline 4-ID of the National Synchrotron Light Source II, a U.S. Department of Energy (DOE) Office of Science User Facility operated for the DOE Office of Science by Brookhaven National Laboratory under Contract No. DE-SC0012704. Use of the APS was supported by the US Department of Energy, Office of Science, Basic Energy Sciences, under Contract No. DE-AC02-06CH11357.

[1] L. Balents, *Nature* **464**, 199 (2010).
 [2] A. Kitaev, *Annals of Physics* January Special Issue, **321**, 2 (2006).
 [3] G. Jackeli and G. Khaliullin, *Phys. Rev. Lett.* **102**, 017205 (2009).
 [4] J. Chaloupka, *Phys. Rev. Lett.* **105**, 10.1103/PhysRevLett.105.027204 (2010).
 [5] Y. Matsuda, T. Shibauchi, and H.-Y. Kee, *Rev. Mod. Phys.* **97**, 045003 (2025).
 [6] K. W. Plumb, J. P. Clancy, L. J. Sandilands, V. V. Shankar, Y. F. Hu, K. S. Burch, H.-Y. Kee, and Y.-J. Kim, *Phys. Rev. B* **90**, 041112 (2014).
 [7] Y. Singh and P. Gegenwart, *Phys. Rev. B* **82**, 064412 (2010).
 [8] Y. Singh, S. Manni, J. Reuther, T. Berlijn, R. Thomale, W. Ku, S. Trebst, and P. Gegenwart, *Phys. Rev. Lett.* **108**, 127203 (2012).
 [9] S. M. Winter, A. A. Tsirlin, M. Daghofer, J. van den Brink, Y. Singh, P. Gegenwart, and R. Valentí, *J. Phys.: Condens. Matter* **29**, 493002 (2017).
 [10] A. Biffin, R. Johnson, I. Kimchi, R. Morris, A. Bombardi, J. Analytis, A. Vishwanath, and R. Coldea, *Phys. Rev. Lett.* **113**, 197201 (2014).
 [11] A. Biffin, R. D. Johnson, S. Choi, F. Freund, S. Manni, A. Bombardi, P. Manuel, P. Gegenwart, and R. Coldea, *Phys. Rev. B* **90**, 205116 (2014).
 [12] S. Williams, R. Johnson, F. Freund, S. Choi, A. Jesche, I. Kimchi, S. Manni, A. Bombardi, P. Manuel, P. Gegenwart, and R. Coldea, *Phys. Rev. B* **93**, 195158 (2016).
 [13] X. Liu, T. Berlijn, W.-G. Yin, W. Ku, A. Tsvelik, Y.-J. Kim, H. Gretarsson, Y. Singh, P. Gegenwart, and J. P. Hill, *Phys. Rev. B* **83**, 220403 (2011).
 [14] J. A. Sears, M. Songvilay, K. W. Plumb, J. P. Clancy, Y. Qiu, Y. Zhao, D. Parshall, and Y.-J. Kim, *Phys. Rev. B* **91**, 144420 (2015).
 [15] J. G. Rau, E. K.-H. Lee, and H.-Y. Kee, *Phys. Rev. Lett.* **112**, 077204 (2014).
 [16] K. A. Modic, T. E. Smidt, I. Kimchi, N. P. Breznay, A. Biffin, S. Choi, R. D. Johnson, R. Coldea, P. Watkins-Curry, G. T. McCandless, J. Y. Chan, F. Gandara, Z. Islam, A. Vishwanath, A. Shekhter, R. D. McDonald, and J. G. Analytis, *Nat Commun* **5**, 4203 (2014).
 [17] A. Ruiz, V. Nagarajan, M. Vranas, G. Lopez, G. T. McCandless, I. Kimchi, J. Y. Chan, N. P. Breznay, A. Frañó, B. A. Frandsen, and J. G. Analytis, *Phys. Rev. B* **101**, 075112 (2020).
 [18] A. Ruiz, A. Frano, N. P. Breznay, I. Kimchi, T. Helm, I. Oswald, J. Y. Chan, R. Birgeneau, Z. Islam, and J. G. Analytis, *Nature Communications* **8**, 961 (2017).
 [19] M. Majumder, R. Manna, G. Simutis, J. Orain, T. Dey, F. Freund, A. Jesche, R. Khasanov, P. Biswas, E. Bykova, N. Dubrovinskaia, L. Dubrovinsky, R. Yadav, L. Hozoi, S. Nishimoto, A. Tsirlin, and P. Gegenwart, *Phys. Rev. Lett.* **120**, 237202 (2018).
 [20] B. Shen, A. Jesche, M. L. Seidler, F. Freund, P. Gegenwart, and A. A. Tsirlin, *Phys. Rev. B* **104**, 134426 (2021).
 [21] Y.-Z. You, I. Kimchi, and A. Vishwanath, *Phys. Rev. B* **86**, 085145 (2012).
 [22] S. Okamoto, *Phys. Rev. B* **87**, 064508 (2013).
 [23] J. Schmidt, D. D. Scherer, and A. M. Black-Schaffer, *Phys. Rev. B* **97**, 014504 (2018).
 [24] E. C. Andrade and M. Vojta, *Physical Review B* **90**, 205112 (2014).
 [25] W. P. Cai, Z. R. Yan, R. M. Liu, M. H. Qin, M. Zeng, X. B. Lu, X. S. Gao, and J.-M. Liu, *Journal of Physics: Condensed Matter* **29**, 405806 (2017).
 [26] K. Mehlawat, G. Sharma, and Y. Singh, *Phys. Rev. B* **92**, 134412 (2015).
 [27] A. J. Willans, J. T. Chalker, and R. Moessner, *Phys. Rev. Lett.* **104**, 237203 (2010).
 [28] K. Dhochak, R. Shankar, and V. Tripathi, *Phys. Rev. Lett.* **105**, 117201 (2010).
 [29] K. Rolfs, S. Toth, E. Pomjakushina, D. Sheptyakov, J. Taylor, and K. Conder, *Phys. Rev. B* **91**, 180406

(2015).

[30] S. Manni, S. Choi, I. I. Mazin, R. Coldea, M. Altmeyer, H. O. Jeschke, R. Valentí, and P. Gegenwart, Phys. Rev. B **89**, 245113 (2014).

[31] G. Cao, T. F. Qi, L. Li, J. Terzic, V. S. Cao, S. J. Yuan, M. Tovar, G. Murthy, and R. K. Kaul, Phys. Rev. B **88**, 220414 (2013).

[32] S. Manni, Y. Tokiwa, and P. Gegenwart, Phys. Rev. B **89**, 241102 (2014).

[33] H. Lei, W.-G. Yin, Z. Zhong, and H. Hosono, Phys. Rev. B **89**, 020409 (2014).

[34] J. C. Wang, J. Terzic, T. F. Qi, F. Ye, S. J. Yuan, S. Aswartham, S. V. Streltsov, D. I. Khomskii, R. K. Kaul, and G. Cao, Phys. Rev. B **90**, 161110 (2014).

[35] G. Jackeli and D. I. Khomskii, Phys. Rev. Lett. **100**, 147203 (2008).

[36] S. A. J. Kimber, Phys. Rev. B **89**, 10.1103/PhysRevB.89.081408 (2014).

[37] A. D. Hillier, S. J. Blundell, I. McKenzie, I. Umegaki, L. Shu, J. A. Wright, T. Prokscha, F. Bert, K. Shimomura, A. Berlie, H. Alberto, and I. Watanabe, Nat. Rev. Methods Primers **2**, 4 (2022).

[38] P. Nordblad, P. Svedlindh, L. Lundgren, and L. Sandlund, Phys. Rev. B **33**, 645 (1986).

[39] Y. Uemura, in *Muon Science: Muons in Physics, Chemistry and Materials*, edited by S. Lee, R. Cywinski, and S. Kilcoyne (Taylor & Francis, New York, 1999).

[40] S. J. Blundell, Contemp. Phys. **40**, 175 (2010).

[41] G. Bastien, M. Roslova, M. H. Haghghi, K. Mehlawat, J. Hunger, A. Isaeva, T. Doert, M. Vojta, B. Büchner, and A. U. B. Wolter, Phys. Rev. B **99**, 214410 (2019).

[42] H. Roux-Buisson and J. M. D. Coey, J. Phys. F: Met. Phys. **10**, 275 (1980).

[43] D. X. Li, Y. Shimizu, A. Nakamura, Y. J. Sato, Y. Homma, F. Honda, and D. Aoki, Journal of Magnetism and Magnetic Materials **562**, 169820 (2022).

[44] X. Yin, C. Xu, Q. Lu, J. Li, R. Feng, F. Liu, Z. Liu, B. Zhang, C. Chen, L. Chen, S. Huang, J. Jiao, B. Zhao, J. Zhao, Y. Cao, G. Wang, J. Ma, and D. Qian, Phys. Rev. B **110**, 144422 (2024).

[45] A. Ruiz, N. P. Breznay, M. Li, I. Rousochatzakis, A. Allen, I. Zinda, V. Nagarajan, G. Lopez, Z. Islam, M. H. Upton, J. Kim, A. H. Said, X.-R. Huang, T. Gog, D. Casa, R. J. Birgeneau, J. D. Koralek, J. G. Analytis, N. B. Perkins, and A. Frano, Phys. Rev. B **103**, 184404 (2021).